1   **Permeability and elastic properties of rocks from the northern Hikurangi margin:**
2   **Implications for slow-slip events**

3   **Nicola Tisato[1], Carolyn D. Bland[1*], Harm Van Avendonk[2], Nathan Bangs[2], Hector Garza[1],**
4   **Omar Alamoudi[1], Kelly Olsen[2†], Andrew Gase[2‡]**

5   [1] Department of Earth and Planetary Sciences, Jackson School of Geosciences, The University of
6   Texas at Austin, Austin, TX, U.S.

7   [3] Institute for Geophysics, Jackson School of Geosciences, The University of Texas at Austin,
8   Austin, TX, U.S.

9   [*] Now at: Pariveda Solutions, Dallas, TX, U.S.

10   [†] Now at: Descartes Labs, 1607 Paseo de Peralta, Suite B, Sante Fe, NM, U.S.

11   [‡] Now at: Geology Department, Western Washington University, Bellingham, WA, U.S.

12

13   Corresponding author: Nicola Tisato (nicola.tisato@jsg.utexas.edu)
14

FB12

38.2967 S WGS 84
178.0989 E WGS 84

L 26.32±0.05 mm
D 24.99±0.108 mm
ρ 2.23±0.05 g/cm^3
Φ 17.84±2.04 %

GB13

38.6498 S WGS 84
178.1467 E WGS 84

L 45.1±0.05 mm
D 25.01±0.169 mm
ρ 2.27±0.07 g/cm^3
Φ 15.64±2.62 %

MT07

38.3709 S WGS 84
177.6008 E WGS 84

L 62.02±0.01 mm
D 25.18±0.04 mm
ρ 2.49±0.01 g/cm^3
Φ 6.83±0.41 %

MO02

38.6178 S WGS 84
177.4545 E WGS 84

L 51.47±0.03 mm
D 25.13±0.05 mm
ρ 2.51±0.02 g/cm^3
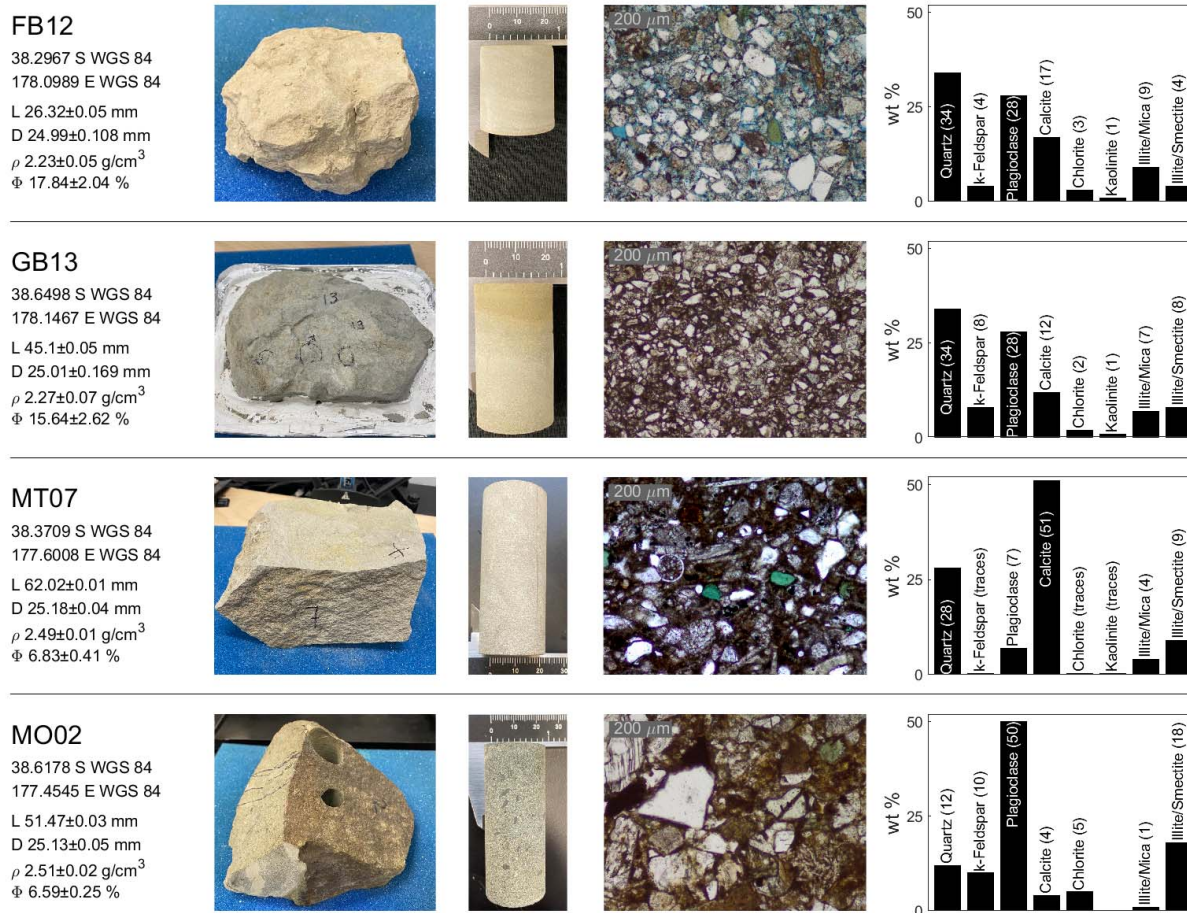Φ 6.59±0.25 %

Figure S1. For each sample, the left column reports the geographic coordinates, length (L), diameter (D), density (ρ), and porosity (Φ). The three center columns are pictures of hand samples and transmitted light microphotographs. The right column reports mineral compositions according to X-ray diffraction analyses (XRD).

Sample preparation details

The end faces of each core plug were smoothed to parallel using a rock saw and a lathe equipped with an angular grinder. Parallelism was checked with a 0.01 mm resolution caliper. Each core was oven-dried at ~333 K for several days to reduce absorbed water. We then calculated the total volume and density of each core by measuring its mass and dimensions using a scale and a caliper to accuracies of 0.001 g and 0.02 mm, respectively. A helium pycnometer (Micromeritics AccuPyc II 1340) was used to measure the solid volume and porosity of each core.

To evenly distribute the saturating water or the helium gas to test permeability across the sample end-face, we placed 3.175 mm thickness, 10 µm grain size, AISI 316 stainless steel porous frits between each sample holder and the adjacent sample end-face.

Sample MT07 at stage S3 - i.e., fractured after being exposed to humidity - was epoxy impregnated before removing the rubber jacket to avoid offsetting the fracture.

Preparation of the saturating water for sample GB13

Water chemically equilibrated with sample GB13 was prepared and injected as follows: For several weeks before saturation, we submerged a few grams of GB13 granules in deionized water. Then, the injection of such aqueous fluid was performed using a high-pressure syringe pump (ISCO 260HP), recording – via a Matlab script - the injected volume and injection pressure. The latter was maintained constant to a value of 3 MPa lower than the confining pressure that varied between 20 and 50 MPa.

Ultrasonic and mechanical testing details

Our samples have a maximum ultrasonic velocity of ~6 km/s and considering the testing frequency of 800 kHz, we estimated a maximum wavelength (λ_M) of 7.5 mm and, to avoid nearfield effects, we prepared cores with a length (L) > 3 λ_M. Velocities were estimated with the transmission method by measuring the time of travel of the elastic wave along the core plug (Birch, 1960). We corrected the first arrival by the delay introduced by the sample holders that was determined by a standard calibration procedure (e.g., Prelicz, 2005). A pulser-receiver apparatus (JSR Ultrasonics DPR300) generated a negative spike pulse with a typical duration of ~40 ns feeding the source ultrasonic transducer. We used a pulsing rate of 100 pulses/sec (PRF RATE=1), pulse amplitude of ~194 V (PULSE AMPLITUDE = 4, and PULSE ENERGY = HIGH Z 4), and damping of 331 Ohms (DAMPING = 1). In addition, the pulser-receiver produces a trigger signal (5 V in amplitude) to synchronize the pulser and the oscilloscope (Rigol DS1104Z-S) collecting the signals generated by the receiving transducer and amplified by the receiver. The latter has a gain of 66 dB (REL. GAIN = 79), a high-pass filter corner frequency of 1 MHz, and a low-pass filter corner frequency of 3 MHz. Two data transfer switches allow selecting the recording of the V_P, V_{S1} or V_{S2} signal. To improve the signal-to-noise ratio the oscilloscope collects and stacks 1024 signals and transmits the digitized wavelets to a computer via a USB port. Typically, the signal, comprising 1200 samples, is digitized every 0.2 μs or less and saved as a comma-separated-value (CSV) file. Shear velocities were calculated as the average of V_{S1} and V_{S2}.

All velocities (V) as a function of σ_M were fit according to Eberhart-Phillips et al., 1989:

$$V = a + k\,\sigma_M - b\,e^{-d\,\sigma_M} \qquad \text{eq. S1}$$

Where a, k, b, and d are fitting parameters. Table S1 reports the fitting parameters for all the measurements reported in Figure 2A. As σ_M increases, especially above ~50 MPa, the effect of the non-linear part of eq. S1 decreases, and V tends to be equal to:

$$V = a + k\,\sigma_M \qquad \text{eq. S2}$$

The exponential increase of velocity (e.g., $-b\,e^{-d\,\sigma_M}$) is controlled by crack closure (e.g., Eberhart-Phillips et al., 1989; Tsuji & Iturrino, 2008). Cracks are naturally occurring, but some of our sample cracks were probably produced during preparation. Therefore, the measured velocities and those modeled with eq. S1 possibly underestimate the velocities of the undisturbed rocks. On the other end, the velocities calculated according to eq. S2 represent an upper bound for the undisturbed rock velocities. Therefore, to provide a range of possible velocities, table S2 reports values calculated according to eqs. S1 and S2, and we used their average to color code the symbols in Figure 4B, which compares ultrasonic and seismic velocities in section MC10 (fig. 4A).

We estimated the ultrasonic wave velocities of the saturated sample GB13 (wet) using the Gassmann fluid substitution (Gassmann, 1951). We obtained the dry bulk and shear modulus from the measured ultrasonic velocities and density. We used a porosity of 15.64% and estimated

the effective bulk modulus of the mineral material making up the rock (K_0=41.9 GPa) using the Voigt-Reuss-Hill average (Hill, 1952). Such an average was calculated considering the mineral abundances and bulk moduli in Table S3.

Samples compaction was measured to 1 µm accuracy with a Linear Variable Displacement Transducer connected to the axial piston, whose signal was acquired along with the confining pressure and vertical force.

Sample	Vp a, km/s	Vp k, km/(s MPa)	Vp b, km/s	Vp d, 1/MPa	Vs a, km/s	Vs k, km/(s MPa)	Vs b, km/s	Vs d, 1/MPa
MT07	4.259	0.00040	0.5508	0.01559	2.287	0.00040	0.0979	0.0403
MO02	4.833	0.00048	0.9625	0.01998	2.671	0.00107	0.3333	0.0469
FB12	3.411	0.00149	0.8080	0.01892	1.935	0.00052	0.6075	0.0280
FB12 compacted	3.655	0.00221	0.6489	0.01697	2.087	0.00048	0.5253	0.0135
GB13 dry	3.198	0.00040	0.6979	0.05500	1.925	0.00040	0.3755	0.0530
GB13 wet	3.120	0.00453	0.4441	0.30994	1.598	0.00370	0.0215	0.0301

Table S1: Fitting parameters for the samples ultrasonic velocities according to eqs. S1 and S2.

Sample	Φ, %	κ, m2	σM, MPa	Vp (meas.) km/s	Vp (EP89) min, km/s	Vp (EP89) max, km/s	Vp (EP89) mean, km/s
FB12	17.3	3.95E-16	10	2.788	2.757	3.426	3.092
FB12	16.0	3.52E-16	20	2.937	2.887	3.441	3.164
FB12	15.6	3.04E-16	30	2.986	2.998	3.456	3.227
FB12	13.7	1.63E-16	50	3.055	3.172	3.486	3.329
FB12	13.4	1.24E-16	70	3.251	3.301	3.515	3.408
FB12	14.1	2.60E-16	30	2.968	2.998	3.456	3.227
FB12	14.4	3.38E-16	20	2.895	2.887	3.441	3.164
FB12 compacted	14.0	2.13E-17	30	3.333	3.331	3.721	3.526
FB12 compacted	14.0	1.46E-17	70	3.543	3.611	3.809	3.710
FB12 compacted	11.7	5.97E-18	150	3.866	3.935	3.986	3.961
FB12 compacted	10.3	3.64E-18	200	4.008	4.075	4.097	4.086
FB12 compacted	10.3	5.10E-18	150	3.863	3.935	3.986	3.961
FB12 compacted	10.4	5.56E-18	100	3.745	3.757	3.876	3.816
FB12 compacted	10.4	8.67E-18	70	3.618	3.611	3.809	3.710
FB12 compacted	11.2	1.54E-17	30	3.298	3.331	3.721	3.526
MO02	5.9	8.47E-20	30	4.353	4.320	4.848	4.584
MO02	5.5	7.80E-21	50	4.479	4.502	4.857	4.680
MT07	6.4	2.03E-20	30	3.838	3.926	4.271	4.098
MT07	6.2	1.39E-20	50	3.913	4.026	4.279	4.153
MT07	6.0	6.29E-21	70	3.995	4.102	4.287	4.194
MT07	6.4	1.92E-20	20	3.843	3.864	4.267	4.065

Table S2: Porosity, permeability, mean stress, and Vp for our sample data that are reported in Figure 4B. 'Vp (meas.)' indicate the measurements, 'Vp (EP89) min' is the velocity estimated using eq. S1, 'Vp (EP89) max' is the velocity estimated according to eq. S2. 'Vp (EP89) mean' is the average between 'Vp (EP89) min' and 'Vp (EP89) max'. The latter is used to color-code the symbols of samples MT07, MO02, and FB12 in Figure 4B.

Mineral	Fraction	Bulk Modulus	
Quartz	34%	37.0	GPa
K-feldspar	8%	37.5	GPa
Plagioclase	28%	76.0	GPa
Calcite	12%	77.0	GPa
Clays	18%	15.0	GPa

Table S3. Parameters used to calculate the effective bulk modulus of the minerals making up sample GB13 (K_0). Fractions are estimated from XRD (see Figure S1), and bulk moduli are taken from (Carmichael, 1989).

Permeability testing

The two reservoirs connected to the sample end-faces have volumes V_1=58.725 ml and V_2=162.53 ml, and at the beginning of the test, we connected the reservoirs to a high-pressure helium gas bottle to raise their internal pressures to two different values $P_{1i} > P_{2i}$. While P_{1i} is greater than P_{2i}, helium flows through the sample until pressure equilibrium is reached. Two digital manometers (Keller LEO3) connected to a computer and a Matlab code record P1 and P2 over time (t). The two manometers also measure temperature (T). Permeability is then calculated as:

$$\kappa = -\frac{\beta \, \eta \, L}{\left(\frac{1}{V_1}+\frac{1}{V_2}\right) K \, A}, \qquad \text{eq. S3}$$

Where η and K are Helium viscosity and bulk modulus, respectively; L and A are the lengths and cross-section area of the sample; β is the exponent of the pressure decay:

$$P_1 = (P_{1i} - P_{2i}) \, e^{\beta \, t} + P_f, \quad \text{eq. S4}$$

Where P_f is the equilibrium pressure, i.e., P_1 and P_2 at time infinite. We assume helium properties as a function of pressure and temperature from the national institute for standards and technology (NIST) fluid thermophysical properties (Arp et al., 1998; Ortiz-Vega et al., 2020). P_f and β were estimated by means of a non-linear least absolute residuals fit implemented in Matlab.

XRD and CT-scanner setup

Mineralogical X-ray diffraction analyses were conducted at the Geomaterials Characterization and Imaging Facility (GeoMatCl) at The University of Texas at Austin. Whole rock samples were manually homogenized, ground, and sieved to a 250 μm mesh size. XRD analyses were performed using a Bruker D8 diffractometer instrument equipped with Cu Kα radiation and a nickel filter, along with a LYNXEYE solid-state detector. The analyses were carried out at a voltage of 45 kV and a current of 40 mA, employing a 2θscan axis ranging from 3° to 70°, with step increments of .0195° (2θ) and a duration of 1 s per step. Whole rock X-ray patterns (Fig S2) were determined through Rietveld refinement utilizing Bruker TOPAS 4.2 software.

For clay speciation analyses (Fig S3), we followed the modified methods based on Hillier (2000) and Moore & Reynolds (1997). CaCO$_3$ rich samples were subjected to a modified HCl-Na$_2$CO$_2$ treatment (5% diluted HCl) to disseminate clay minerals following the method of Komadel et al. (1990) and Meredith E. Ostrom (1961). Disaggregated material was separated into a <2-micron clay fraction suspension using sodium hexametaphosphate, enabling the

acquisition of clay speciation by excluding heavier non-phyllosilicate minerals. The <2-micron clay suspension was vacuum-filtered through a millipore filter and subsequently oriented onto a glass slide. The oriented clay mounts were subjected to ethylene glycol vapors for 24 hours, followed by heating (1 hour) to 400°C to identify swelling clays. Clay speciation X-ray patterns with a 2θ scan axis ranging from 3° to 70°, with step increments of 0.195° (2θ) and a duration of 1 s per step were evaluated using reference intensity ratios (RIR), and mineral intensity factors (MIF) with the MDI Jade software.

For CT-scanning we used an NSI scanner equipped with a Fein Focus High Power source, at 120 kV voltage and 0.14 mA current. CT scans were acquired at 33.3 μm per voxel resolution. The X-ray source was filtered using aluminum foil. The CT scanner is equipped with a Perkin Elmer detector, with 0.5 pF gain, and the 1800 projections were collected at 1 fps and 1x1 binning. The source-to-object distance was 150.566 mm, and the source to detector 963.799 mm. We performed a continuous CT scan by averaging 2 frames and by skipping 0 frames. We applied a beam-hardening correction of 0.25 and a post-reconstruction ring correction using the following parameters: oversample = 2, radial bin width = 21, sectors = 32, minimum arc length = 2, angular bin width = 9, angular screening factor = 4. The final reconstructed volume had a voxel size of 33.3 μm and 1873 slices.
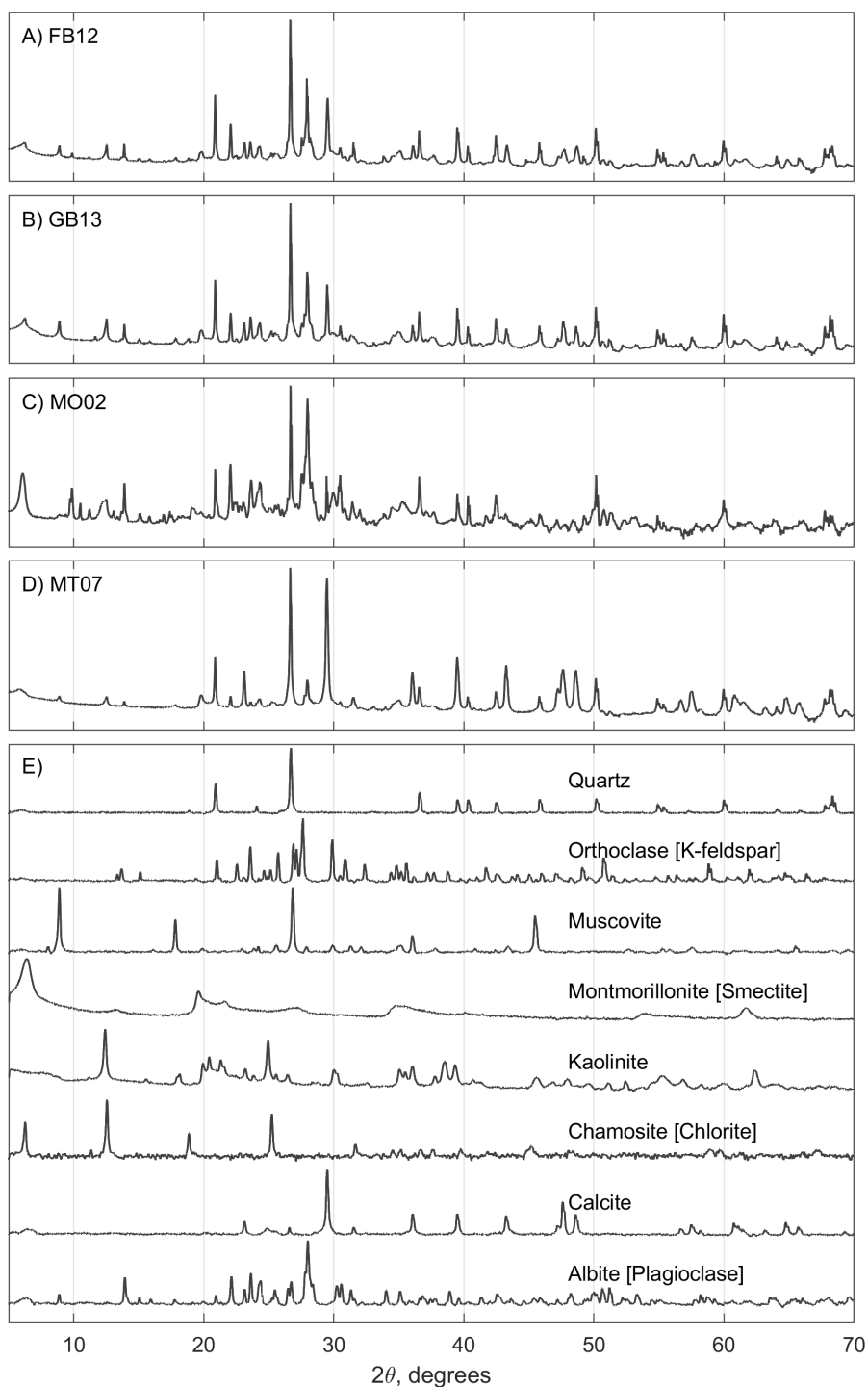
Figure S2. A-D) XRD spectra of the four samples. E) Standard spectra for the mineral comprising our samples. Data have been taken from the RRUFF database (Lafuente et al., 2015): Talc URL=rruff.info/R040137; Quartz URL=rruff.info/R040031; Orthoclase URL=rruff.info/R040055; Muscovite URL=rruff.info/R040104; Montmorillonite URL=rruff.info/R110052; Kaolinite URL=rruff.info/R140004; Chamosite URL=rruff.info/R060188; Calcite URL=rruff.info/R040070; Albite URL=rruff.info/R040068.
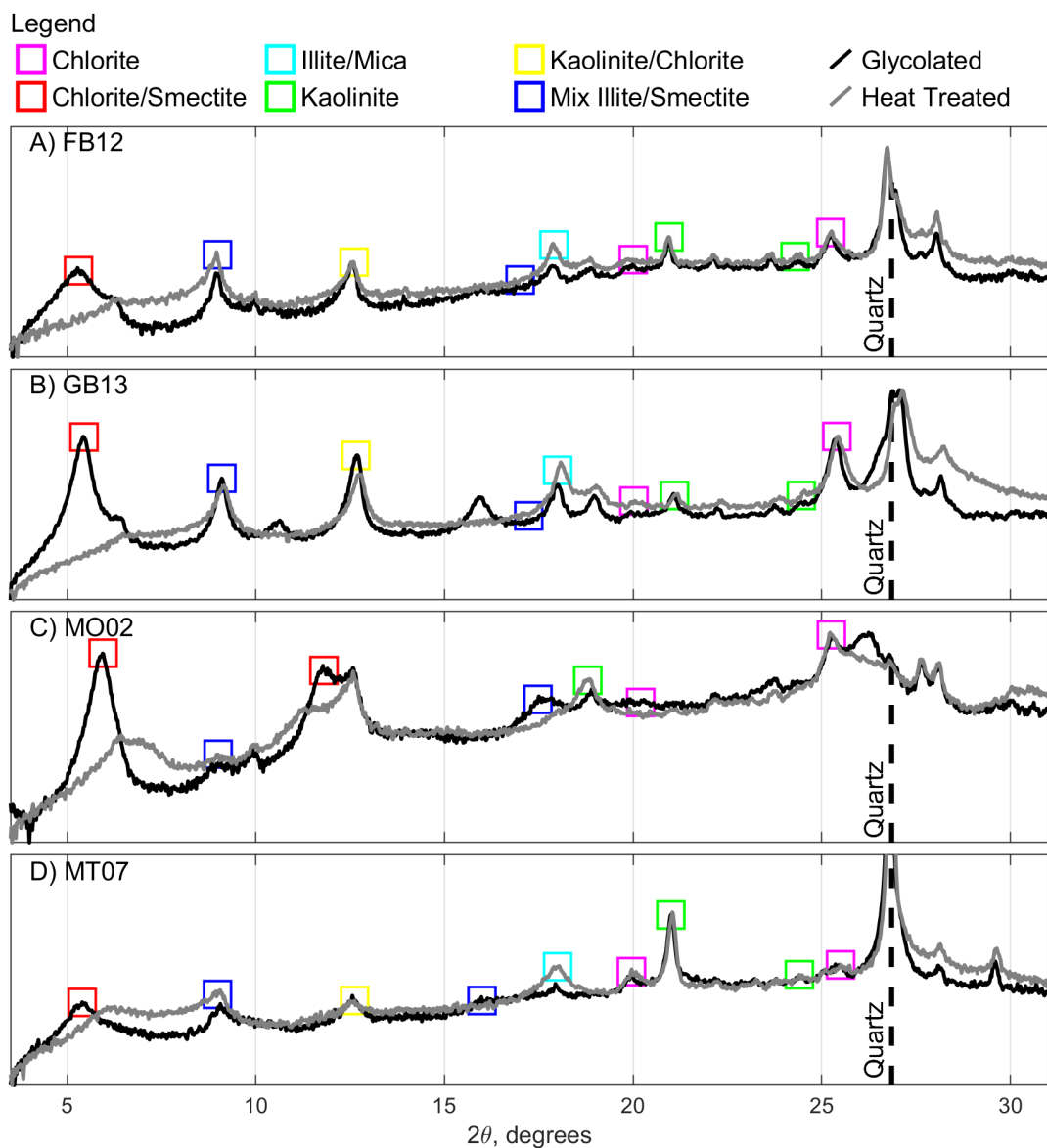
Figure S3. XRD clay patterns (oriented, glycolated, heat-treated at 400°C) for Illite/Mica, Mix Illite/Smectite, Kaolinite, and Chlorite minerals. Squares indicate peaks and portions of spectra used to speciate and estimate clay fractions for each sample.

A) Sample FB12 is dominated by Illite/Mica, followed by Mix Illite/Smectite, with minor quantities of Chlorite and Kaolinite. B) Sample GB13 exhibits an abundance of Mix Illite/Smectite and Illite/Mica, along with trace amounts of Chlorite and Kaolinite. C) Sample MO02 is notably rich in Mix Illite/Smectite, with a significant presence of Chlorite and minor content of Illite/Mica.

D) Sample MT07 is primarily rich in Mix Illite/Smectite, featuring a notable abundance of Illite/Mica, and minor quantities of Chlorite and Kaolinite.

Fracture aperture calculation

To normalize CT-scan datasets, we fit a Gaussian function to the distribution of CT numbers to obtain a CT-number mean (m_x) and standard deviation (s_x), where x is either S1, S2,

or S3. To compare datasets acquired at different stages, we shifted the CT-numbers of datasets S2 and S3 by m_{S1}-m_{S2} and m_{S1}-m_{S3}, respectively. We added a value of 1 to each voxel, cropped each image to 718x718 pixels around the sample center, and assigned a value of 0 to pixels with a distance >718/2 from the sample center. We binarized the datasets to assign each voxel to either solid rock or air by applying a threshold calculated as:

$$t_x = m_x - 2.5\, s_x \qquad \text{eq. S5}$$

Voxels with CT-number equal to or greater than t_x were assumed to represent rock and assigned a value of 255. Voxels with CT-number lower than t_x and greater than zero were assumed to be air and assigned a value of 128.

To obtain a FADP of a binarized dataset, we calculated: 1) The Euclidian distance of each voxel in the fracture. This is achieved by a) performing an iterative image morphological erosion assigning approximated distances of each fracture voxel from the fracture rim, and b) calculating the Euclidian distance of each voxel within the fracture from the closest voxel representing rock; 2) The skeleton of the fracture (SK) comprises the voxels that are within the fracture and have the maximum Euclidian distance from the fracture rim into respect the 26 surrounding voxels. Such a device extracts the center surface while preserving the topology and Euler number, also known as the Euler characteristic of the objects (Kerschnitzki et al., 2013; Lee et al., 1994). Finally, the FADP was calculated at each SK location by doubling the Euclidian distance recorded in such voxels.

References

Arp, V. D., McCarty, R. D., & Friend, D. G. (1998). *Thermophysical Properties of Helium-4 from 0.8 to 1500 K with Pressures to 2000 MPa* (Technical Report No. 1334 (revised)). NIST.

Birch, F. (1960). The velocity of compressional waves in rocks to 10 kilobars: 1. *Journal of Geophysical Research*, *65*(4), 1083–1102. https://doi.org/10.1029/JZ065i004p01083

Carmichael, R. S. (Ed.). (1989). *Practical handbook of physical properties of rocks and minerals*. Boca Raton, Fla: CRC Press.

Eberhart-Phillips, D., Han, D.-H., & Zoback, M. D. (1989). Empirical relationships among seismic velocity, effective pressure, porosity, and clay content in sandstone. *GEOPHYSICS*, *54*(1), 82–89. https://doi.org/10.1190/1.1442580

Gassmann, F. (1951). Elastic waves through a packing of spheres. *GEOPHYSICS*, *16*(4), 673–685. https://doi.org/10.1190/1.1437718

210   Hill, R. (1952). The Elastic Behaviour of a Crystalline Aggregate. *Proceedings of the Physical*

211   *Society. Section A*, *65*(5), 349–354. https://doi.org/10.1088/0370-1298/65/5/307

212   Hillier, S. (2000). Accurate quantitative analysis of clay and other minerals in sandstones by

213   XRD: comparison of a Rietveld and a reference intensity ratio (RIR) method and the

214   importance of sample preparation. *Clay Minerals*, *35*(1), 291–302.

215   https://doi.org/10.1180/000985500546666

216   Kerschnitzki, M., Kollmannsberger, P., Burghammer, M., Duda, G. N., Weinkamer, R.,

217   Wagermaier, W., & Fratzl, P. (2013). Architecture of the osteocyte network correlates

218   with bone material quality: OSTEOCYTE NETWORK ARCHITECTURE

219   CORRELATES WITH BONE MATERIAL QUALITY. *Journal of Bone and Mineral*

220   *Research*, *28*(8), 1837–1845. https://doi.org/10.1002/jbmr.1927

221   Komadel, P., Schmidt, D., Madejová, J., & Číčel, B. (1990). Alteration of smectites by

222   treatments with hydrochloric acid and sodium carbonate solutions. *Applied Clay Science*,

223   *5*(2), 113–122. https://doi.org/10.1016/0169-1317(90)90017-J

224   Lafuente, B., Downs, R. T., Yang, H., & Stone, N. (2015). 1. The power of databases: The

225   RRUFF project. In T. Armbruster & R. M. Danisi (Eds.), *Highlights in Mineralogical*

226   *Crystallography* (pp. 1–30). DE GRUYTER. https://doi.org/10.1515/9783110417104-

227   003

228   Lee, T. C., Kashyap, R. L., & Chu, C. N. (1994). Building Skeleton Models via 3-D Medial

229   Surface Axis Thinning Algorithms. *CVGIP: Graphical Models and Image Processing*,

230   *56*(6), 462–478. https://doi.org/10.1006/cgip.1994.1042

231   Meredith E. Ostrom (2). (1961). Separation of Clay Minerals from Carbonate Rocks by Using

232   Acid. *SEPM Journal of Sedimentary Research*, *Vol. 31*.

233   https://doi.org/10.1306/74D70B1E-2B21-11D7-8648000102C1865D

234   Moore, D. M., & Reynolds, R. C. (1997). *X-ray diffraction and the identification and analysis of*

235   *clay minerals* (2nd ed). Oxford ; New York: Oxford University Press.

236   Ortiz-Vega, D., Hall, K., Holste, J., Arp, V., Harvey, A., & Lemmon, E. (2020). Helmholtz

237   equation of state for helium. *Journal of Physical and Chemical Reference Data*.

238   Prelicz, R. M. (2005). *Seismic anisotropy in peridotites from the Western Gneiss Region*

239   *(Norway): laboratory measurements at high PT conditions and fabric based model*

240   *predictions* [Application/pdf]. ETH Zurich. https://doi.org/10.3929/ETHZ-A-005115293

241   Tsuji, T., & Iturrino, G. J. (2008). Velocity-porosity relationships in oceanic basalt from eastern

242   flank of the Juan de Fuca Ridge: The effect of crack closure on seismic velocity.

243   *Exploration Geophysics*, *39*(1), 41–51. https://doi.org/10.1071/EG08001

244